International Core Journal of Engineering Volume 12 Issue 4, 2026
ISSN: 2414-1895 DOI: 10.6919/ICJE.202604_12(4).0054

Esterified Starch-derived Hard Carbon Anodes as High Initial Coulombic Efficiency Anode Material for Sodium-ion Batteries

Zhexu Tong[a], Deping Xiong[b], and Weizheng Song[c]

School of Physics and Optoelectronic Engineering, Guangdong University of Technology, Guangzhou, Guangdong 510006, China

[a]ZhexuTong @163.com, [b]depingxiong@163.com, [c]songweizheng1213@163.com

Abstract

The widespread adoption of sodium-ion batteries (SIBs) depends heavily on the development of affordable and renewable hard carbon (HC) anodes. While existing HC synthesis methods often rely on complex chemical modifications to boost electrochemical properties, these complicated processes hinder large-scale industrial application. To address this issue, our study presents a cost-effective and green HC material derived from an esterified cassava starch precursor. We comprehensively evaluated how this specific precursor influences the material's microstructural evolution, surface oxygen functionalities, and over all Na-ion storage mechanisms. During electrochemical evaluation, the optimized MA-SCHC-20 anode delivered an impressive reversible capacity of 356.5 $mAhg^{-1}$ at 0.1 C and achieved a remarkable initial coulombic efficiency (ICE) of 90.2%. Even at a high rate of 5 C, it maintained a robust capacity of 195.7 $mAhg^{-1}$. Furthermore, multi-scan-rate cyclic voltammetry was employed to elucidate the underlying sodium storage kinetics.

Keywords

Sodium-ion Battery; Hard Carbon; Starch; Malay Anhydride.

1. Introduction

Lithium-ion batteries (LIBs), with their high energy density and mature industry chain, have dominated the portable electronics and electric vehicle markets over the past decade.[1] However, constrained by resource supply-demand imbalances, lithium carbonate prices have fluctuated sharply, making it difficult to keep the construction costs of large-scale energy storage plants at ideal levels, which limits further application of LIBs in energy storage development.[2] To address the bottleneck of lithium resources, sodium-ion batteries (SIBs) have reemerged as a highly promising alternative due to their notable resource abundance, cost-effectiveness, and excellent electrochemical performance.[3] Due to the intrinsically larger spatial footprint of sodium ions compared to lithium counterparts, graphite-despite its dominance as the standard anode in commercial LIBs-suffers from severe kinetic and thermodynamic limitations when accommodating Na^+.[4-6] In addition, sodium-intercalated compounds in graphite display poor thermodynamic stability, which restricts graphite's application in sodium-based technologies.[5] Therefore, finding and developing novel carbon anode materials with larger interlayer spacing and stronger structural toughness has become a critical scientific challenge that urgently needs to be addressed in the sodium-ion battery field.

Hard carbon (HC) stands out as the most viable alternative to conventional graphite anodes in SIBs, offering favorable specific capacity combined with exceptional long-term cycling endurance. [7-11] While these carbonaceous materials are typically produced via the elevated-temperature carbonization of diverse raw materials, biomass feedstocks have garnered particular interest owing to

ISSN: 2414-1895 DOI: 10.6919/ICJE.202604_12(4).0054

their inherent sustainability and eco-friendly nature. In recent years, research on biomass-derived hard carbon has made significant progress; biomass precursor-derived hard carbons have advantages such as wide availability, low cost, and diverse structures. [12-14] Currently, mainstream biomass-based precursor materials include cellulose, lignin, glucose, starch, etc. [15,16], and are considered renewable and economical precursors for preparing HC. Nevertheless, the direct thermal treatment of biomass often suffers from inevitable structural degradation of the precursors. Such uncontrolled morphological evolution typically yields carbonaceous products with an expanded specific surface area (SSA), thereby significantly deteriorating the initial coulombic efficiency (ICE) of the resulting HC anodes. [17,18] To improve this situation, structural regulation of hard carbon precursors is required.

Starch is one of the most abundant biomasses on Earth; it is widely present in various plants and is extremely pure with few impurities.[19,20] Moreover, starch also has a high carbon content and is one of the very important precursors for producing hard carbon materials.[21] In recent years, hard carbon derived from starch precursors has been widely used as anode material in sodium-ion batteries; most of these have controlled the microstructure of starch through macroscopic regulation, pre-oxidation, or biochemical reactions, thereby altering the microstructure of the resulting hard carbon during high-temperature carbonization.

As a representative example, a specific study by Song and co-workers [22] demonstrated the synthesis of hard carbon from a polysaccharide-esterified starch precursor. By employing a hydrogen-atmosphere reduction process to intentionally modulate the precursor's oxygen levels, the fabricated carbon anode successfully delivered a substantial sodium storage capacity of 369.8 $mAhg^{-1}$, alongside a strong initial Coulombic efficiency (ICE) of 82.5%.

In this work, low-cost and renewable cassava starch was used and esterified with maleic anhydride, and the esterified cassava starch was then carbonized to obtain the final product.

This economically viable and ecologically benign fabrication strategy successfully bypasses the need for complex starch-stabilization procedures. Furthermore, the resulting optimized HC anode delivers outstanding capacity retention over 500 cycles at a rate of 1 C, alongside an exceptional initial Coulombic efficiency (ICE) and elevated specific capacity.

2. Experimental Section

2.1 Material Synthesis

To fabricate the target hard carbon (MA-SCHC-20), cassava starch was initially subjected to ball milling with 20 wt% maleic anhydride to form a homogeneous precursor. This blend underwent a stabilization process in an ambient muffle furnace at 100 °C for 4 h (ramp rate: 2 °C min^{-1}). Following this air-treatment, high-temperature carbonization was carried out in a tubular furnace under a steady N_2 flow, where the sample was heated to 1500 °C for 2 h at an identical ramp rate. For comparative studies, reference materials denoted as MA-SCHC-10 and MA-SCHC-30 were synthesized following identical thermal protocols, utilizing maleic anhydride weight fractions of 10% and 30%, respectively.

2.2 Material Characterization

Morphological and microstructural features of the synthesized samples were elucidated using a Sigma300 scanning electron microscope (SEM), coupled with X-ray diffraction (XRD, XRD-6100; Cu Kα radiation, λ = 0.154056 nm, 40 kV, 30 mA) and a DXR 2xi Raman spectrometer. Furthermore, the surface elemental composition and the evolution of chemical functional groups were probed via K-alpha X-ray photoelectron spectroscopy (XPS) and Nicolet iS10 Fourier transform infrared (FTIR) spectroscopy, respectively.

2.3 Electrochemical Evaluation

To evaluate the electrochemical behaviors, CR2032 coin cells were fabricated. The working electrodes were prepared by dispersing the active material (94 wt%), conductive carbon black (2 wt%), styrene-butadiene rubber (2 wt%), and sodium carboxymethyl cellulose (4 wt%) into deionized

ISSN: 2414-1895 DOI: 10.6919/ICJE.202604_12(4).0054

water. The resulting homogeneous slurry was cast onto a copper current collector and dehydrated in an electric oven at 60 °C for 24 h. After punching the coated foil into 13 mm diameter disks with an areal mass loading of roughly 2 mg cm^{-2}, a secondary vacuum drying step was performed at 60 °C for another 24 h. Cell assembly was executed inside an Ar-filled glovebox. Pure sodium metal served as the counter electrode, separated by a Whatman GF/A glass fiber membrane, with 1.0 M $NaPF_6$ dissolved in 1,2-dimethoxyethane (DME) employed as the electrolyte.

3. Results and Discussion

The microcrystalline structure was analyzed by X-ray diffraction (XRD), as shown in Figure 1a. All diffraction patterns display two broadened peaks at 23° and 43°, corresponding to the (002) and (100) crystal planes, indicating that the material possesses a turbostratic graphene structure. According to Bragg's law $2d\sin\theta = n\lambda$, the interlayer spacings of MA-SCHC-10, MA-SCHC-20, and MA-SCHC-30 calculated from the 2θ values of the (002) peak are 0.379, 0.378, and 0.375 nm, respectively. As documented in prior literature, optimizing the distance between pseudo-graphitic layers is critical for the generation of sodium intercalates. Specifically, an expanded interlayer architecture significantly enhances the reversible insertion and extraction kinetics of Na^+. [23,24].

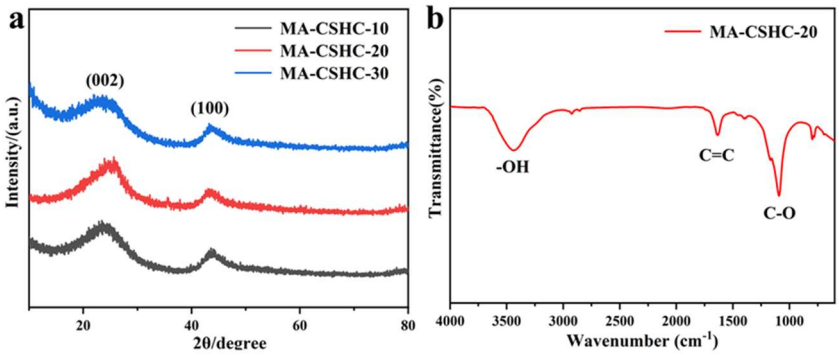

Figure 1. XRD patterns of MA-SCHC-10, MA-SCHC-20 and MA-SCHC-30 (a) and Fourier transform infrared spectra of MA-SCHC-20 (b)

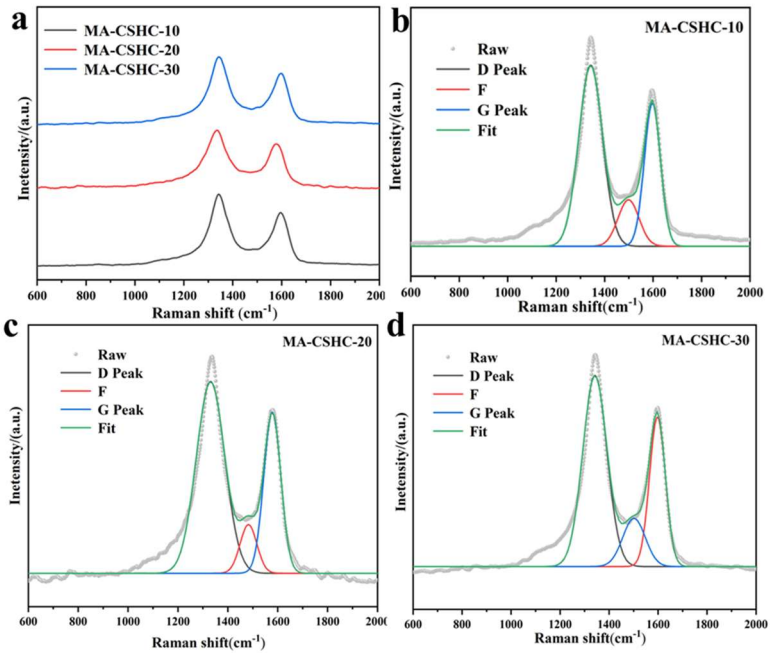

Figure 2. Raman spectra of MA-SCHC-10, MA-SCHC-20 and MA-SCHC-30 (a) and peak fitting (b–d)

ISSN: 2414-1895 DOI: 10.6919/ICJE.202604_12(4).0054

To trace the evolution of oxygenic functionalities following esterification and the subsequent 1500 °C pyrolysis, Fourier transform infrared (FTIR) spectra were recorded. As illustrated in Figure 1b, the MA-SCHC-20 spectrum displays a wide absorption band spanning 3016 to 3696 cm^{-1}, which is classically assigned to O–H stretching modes. Additionally, the resonance feature located at 1632 cm^{-1} reflects the conjugated C=C vibrations within aromatic rings, whereas the distinct signal around 1045 cm^{-1} emerges from the polar stretching of C–O bonds. Collectively, these spectral signatures validate the retention of conventional carbohydrate-like structural motifs.

Raman spectroscopy was performed to probe the structure and defects of these HCs (Figure 2). Each spectrum shows two distinct characteristic peaks at 1350 cm-1 and 1580 cm-1, corresponding to the D peak of disordered structures and the G peak of ordered graphite lattice, respectively [25].The area ratio of the D peak to the G peak (A_D/A_G) is related to the degree of graphitization of carbon materials [26-28].It can be calculated through Gaussian fitting. The AD/AG values of MA-SCHC-10, MA-SCHC-20, and MA-SCHC-30 are 1.32, 1.30, and 1.31, respectively. As the MA content further increases, the A_D/A_G values among the modified samples fluctuate slightly around 1.30, indicating that the contribution of MA to the disorder degree of the carbon skeleton has reached saturation at a mass fraction of 10%.

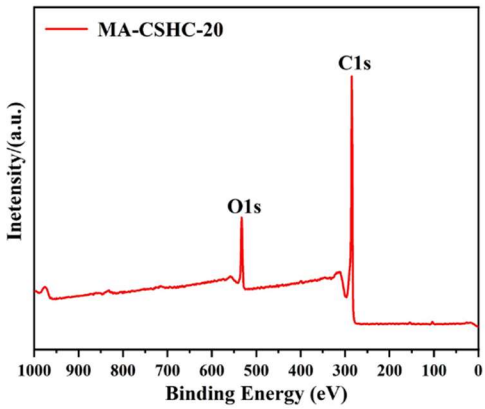

Figure 3. XPS spectrum of MA-SCHC-20

To delve deeper into the surface chemistry of the synthesized samples, X-ray photoelectron spectroscopy (XPS) was employed. As depicted in the survey spectrum (Figure 3), the surface of MA-SCHC-20 is predominantly composed of carbon and oxygen. This is explicitly evidenced by the presence of strong C 1s and O 1s core-level peaks located at approximately 284.8 eV and 532.0 eV (Figure 4), respectively. The complete absence of extraneous elemental signals effectively verifies the high purity of the hard carbon architecture derived via the esterification-carbonization route.

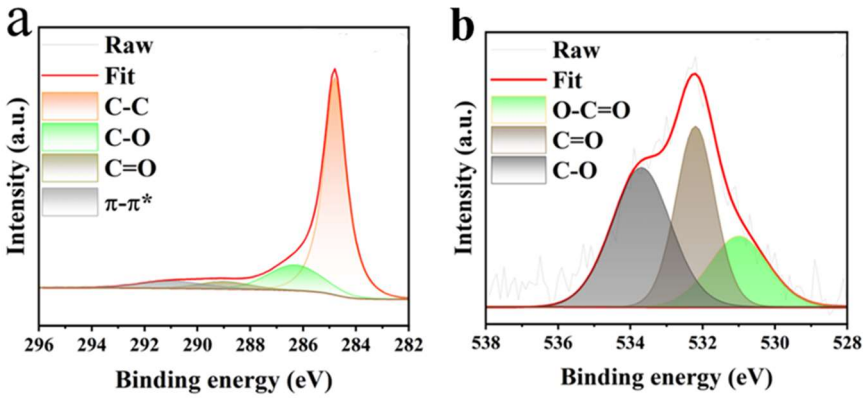

Figure 4. C1s (a) and O1s (b) spectra of MA-SCHC-20

ISSN: 2414-1895 DOI: 10.6919/ICJE.202604_12(4).0054

The effects of different maleic anhydride (MA) addition amounts on the morphology of cassava starch-based hard carbon were observed by SEM. As shown in Figure 5, the variation in modification ratio significantly altered the physical morphology of the final hard carbon. As shown in Figures 5(a-c), MA-SCHC-10 exhibited a dense and continuous bulk structure. At low magnification, larger particle sizes are visible with relatively smooth surfaces (a, b), displaying typical glassy fracture morphology of biomass-derived hard carbon. This indicates that low-content MA esterification primarily functioned as preliminary cross-linking, maintaining the integrity of starch particles after carbonization. As shown in Figures 5(d-f), the morphology of MA-SCHC-20 samples underwent a significant transition, exhibiting distinct porous characteristics. At high magnification (d, e), numerous irregular submicron-scale pores and rough surfaces can be clearly observed. This may be due to the increased MA content intensifying the cross-linking density; however, during the high-temperature-driven dehydrogenation and decarboxylation processes, abundant pore channels were left in the carbon framework due to extensive bond cleavage and gas release. This porous structure is conducive to electrolyte infiltration and rapid sodium ion transport. As shown in Figures 5(g-i), in MA-SCHC-30, as the MA content further increased, the original bulk structure of the material underwent disintegration and refinement. Figure i shows that particle size decreased significantly, presenting fine irregular particle accumulation. This indicates that excessively high MA esterification degree may lead to over-cross-linking of starch molecular chains or overly severe thermal degradation, causing uneven stress distribution during the carbonization process, resulting in macroscopic framework collapse and ultimately forming fine particles with higher specific surface area.

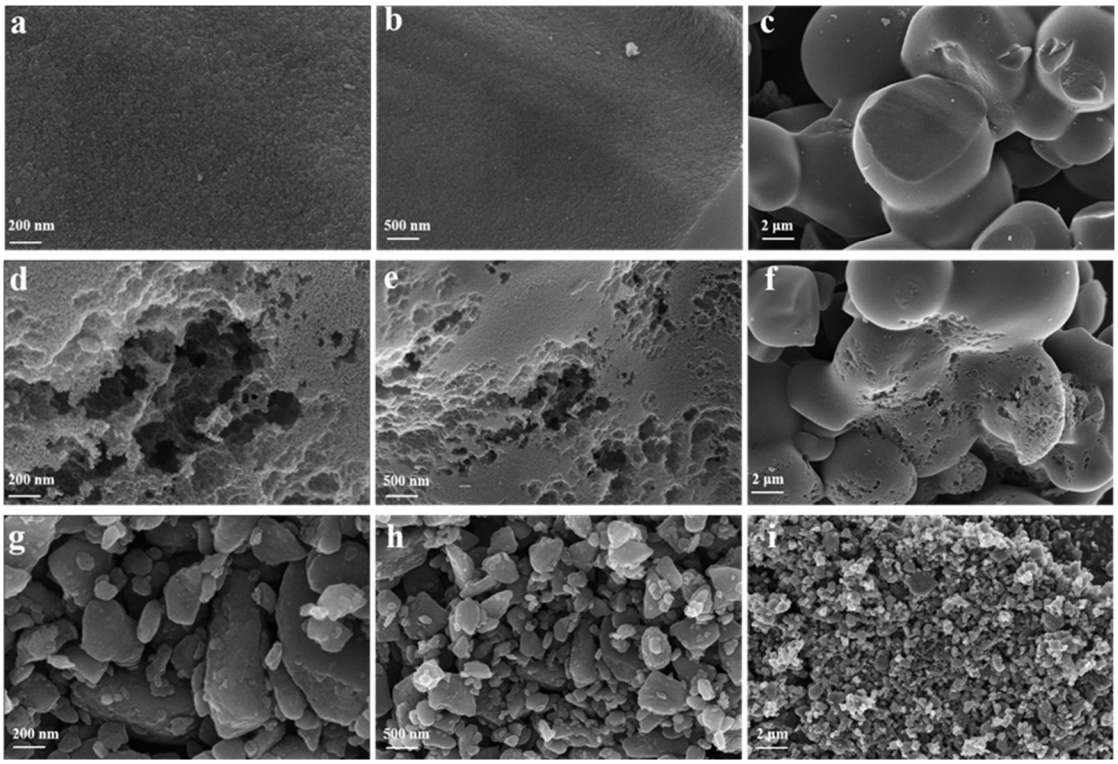

Figure 5. SEM images of MA-SCHC-10 (a–c), MA-SCHC-20 (d-f), and MA-SCHC-30 (h–j)

To systematically evaluate the sodium-storage behaviors, standard CR2032 coin-type half-cells were assembled.

MA-SCHC-20 exhibits the highest reversible specific capacity, with an initial discharge specific capacity of 356.5 $mAhg^{-1}$ and a reversible capacity maintained above 300 $mAhg^{-1}$. In comparison, MA-SCHC-10 has a reversible capacity of only approximately 170 $mAhg^{-1}$, while MA-SCHC-30 is approximately 210 $mAhg^{-1}$.

ISSN: 2414-1895 DOI: 10.6919/ICJE.202604_12(4).0054

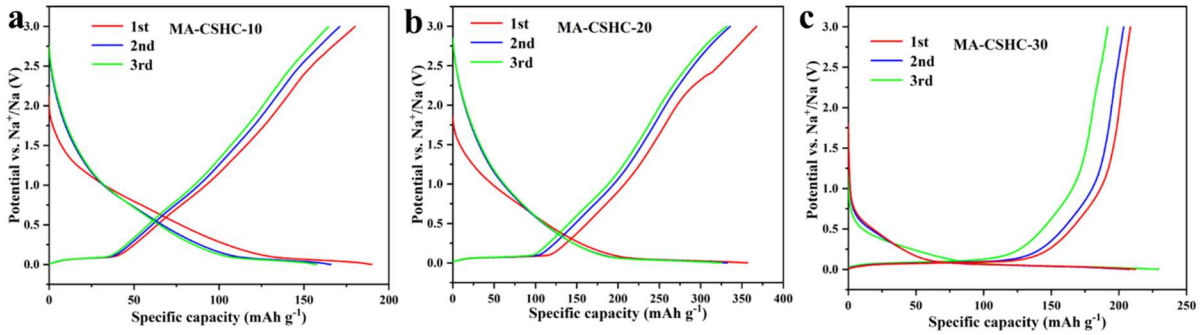

Figure 6. Constant current charge-discharge curves of MA-SCHC-10 (a), MA-SCHC-20 (b), and MA-SCHC-30 (c) anode materials at a current density of 30 mA g^{-1}

MA-SCHC-20 not only exhibits large sloping region capacity but also displays a very pronounced plateau region. In hard carbon theory, the plateau region typically corresponds to the intercalation of sodium ions between graphitized microcrystalline layers. Combined with the previous SEM observations, the abundant porous structure and moderate cross-linking of MA-SCHC-20 generated more accessible closed pores or ordered microcrystalline interlayers, thereby significantly enhancing the plateau region capacity. Although MA-SCHC-30 shows some improvement compared to 10, its capacity is far lower than 20, which is related to the particle fragmentation observed in its SEM. Excessively fine particles lead to reduced structural support, forming excessive open pores, which prevents some sodium ions from being effectively stored through the "pore-filling" mechanism.

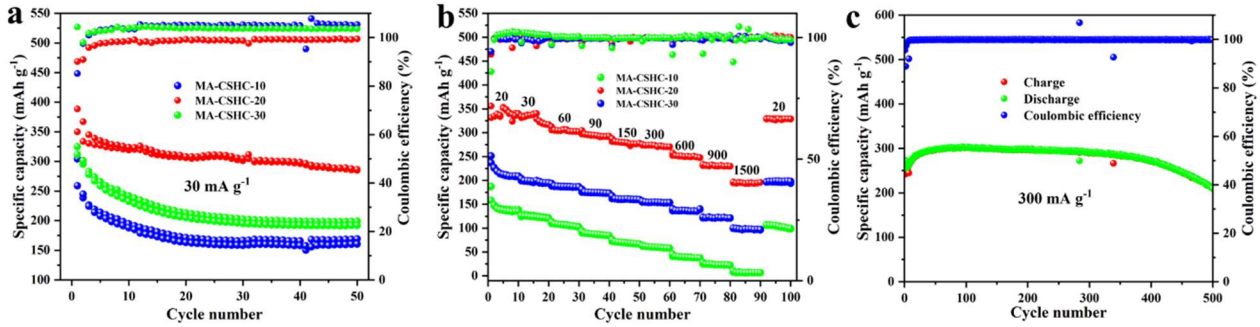

Figure 7. Cycling performance of MA-SCHC-10, MA-SCHC-20 and MA-SCHC-30 at 30 mA g^{-1} (a), rate performance at different scan rates (b), and long-term cycling performance of MA-SCHC-20 at 300 mA g^{-1} (c)

As shown in Figure 7a, at a current density of 30 mA g^{-1}, all three samples exhibited good capacity retention within 50 cycles. Among them, MA-SCHC-20 showed the smoothest cycling curve and maintained a high reversible specific capacity of approximately 300 $mAhg^{-1}$. In comparison, although MA-SCHC-30 had a higher initial capacity than MA-SCHC-10, it showed slightly faster capacity decay, which may be related to the fine particles observed in SEM that expose excessive active sites and lead to continuous SEI growth. The Coulombic efficiency of all samples rapidly approached 100% after the first cycle, indicating good reversibility of the materials. As shown in Figure 7b, the rate capability test demonstrated the superior kinetic advantages of MA-SCHC-20. Under current density gradients ranging from 20 mAg^{-1} to 1500 mAg^{-1}, MA-SCHC-20 consistently maintained the highest specific capacity. Even at the high current density of 1500 mA g^{-1}, its capacity remained around 200 $mAhg^{-1}$, significantly higher than the other two samples. When the current density was restored to 20 mA g^{-1}, its capacity rapidly recovered to the initial level, demonstrating excellent structural resilience of the material framework. This is primarily attributed to the porous structure observed in SEM, which shortens the sodium ion diffusion path and enhances the ion transport rate.

ISSN: 2414-1895 DOI: 10.6919/ICJE.202604_12(4).0054

For the best-performing MA-SCHC-20, long-term cycling stability at a high current of 300 mA g^{-1} was further tested. As shown in Figure 4-9c, after 500 charge-discharge cycles, the material still maintained high capacity with a very smooth curve. This demonstrates that the cross-linked carbon framework formed through maleic anhydride esterification modification possesses excellent mechanical stability and chemical structural stability during long-term sodium ion insertion and extraction, effectively buffering the stress generated by sodium ion embedding and release.

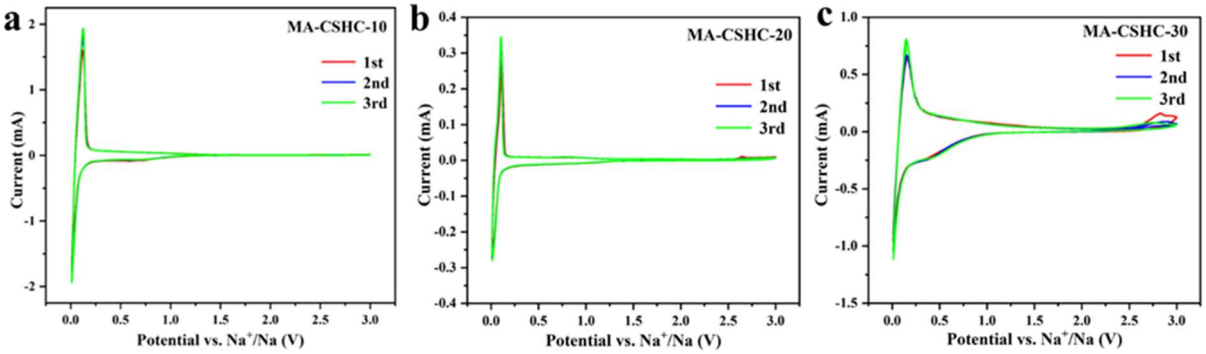

Figure 8. CV curves of MA-SCHC-10(a), MA-SCHC-20(b) and MA-SCHC-30(c) at a scan rate of 0.1 mV/s

Cyclic voltammetry (CV) profiles for the MA-SCHC series, recorded at 0.1 mV s^{-1}, display the classic Na^+ storage signatures expected of hard carbon electrodes (Figure 8). The distinct redox couple observed near 0.01/0.1 V signifies the reversible Na^+ intercalation/deintercalation mechanism, correlating with the voltage plateau. Conversely, the broad humps spanning 0.2–1.2 V represent capacitive-like adsorption at defective sites and functional groups, mirroring the sloping capacity. For the MA-SCHC-30 variant (Figure 8c), the initial cathodic sweep features a broad irreversible current wave between 0.4 and 0.8 V. As corroborated by SEM observations, this prominent electrolyte decomposition and subsequent solid electrolyte interphase (SEI) formation are exacerbated by its reduced particle dimensions and consequent larger electrode-electrolyte interface, ultimately depressing its ICE. In contrast, the MA-SCHC-20 electrode (Figure 8b) demonstrates near-perfect coincidence of its second and third consecutive sweeps. This remarkable superposition, coupled with highly resolved peak profiles, underscores the material's superior structural integrity, exceptional cycling reversibility, and facile Na^+ diffusion kinetics.

To further probe the kinetic dynamics of Na^+ storage within the MA-SCHC-20 architecture, multi-rate cyclic voltammetry was conducted from 0.1 to 2.0 mV s^{-1} (Figure 9). Notably, as illustrated in Figure 9a, elevating the sweep rate induces merely marginal displacements in the redox peak potentials, and the overall voltammogram profiles are robustly maintained. This minimal polarization at accelerated scan velocities serves as a strong indicator of facile charge transfer, confirming the material's superior rate capability and the highly reversible nature of its Na-ion accommodation processes.

Based on the mathematical relationship between peak current and scan rate, the kinetic parameters of the charge transfer process were determined through linear fitting of the cathodic/anodic peaks. According to the formula

$$I = a\, v^b. \quad (1)$$

$$\log(i) = b\log(v) + \log(a). \quad (2)$$

ISSN: 2414-1895 DOI: 10.6919/ICJE.202604_12(4).0054

The sharp oxidation peak (i_a) around 0.1 V and the broad reduction peak (i_r) near the higher potential of 0.3 V in the CV curve were selected for analysis, representing the sodium storage kinetic processes in the plateau region and slope region, respectively. By performing linear fitting on the logarithmic values of the peak response current and scan rate, the b value can be calculated. As shown in Figure 9b, the b value of the cathode peak of the material is 0.41, and the b value of the anode peak is 0.41. This indicates that the electrode reaction of MA-SCHC-20 is dominated by the ion diffusion process, which is consistent with the contribution of the plateau region at low potentials in hard carbon materials.

To quantify the reaction kinetics, the capacitive-controlled fraction at 0.3 mV s^{-1} was calculated to be 45.5% (Figure 9c). This specific capacity primarily originates from the non-peak sloping regions, signifying instantaneous Na^+ adsorption at surface defects and heteroatom-containing edges. Furthermore, escalating the sweep rate from 0.1 to 2.0 mV s^{-1} induces a continuous surge in the capacitive contribution from 37.98% to a dominant 81.32%. Such a progressive evolution implies that under rapid charge/discharge scenarios, sluggish bulk diffusion is bypassed, and the overall capacity is governed by swift surface-confined charge transfer. Consequently, this pronounced pseudocapacitive behavior fundamentally underpins the exceptional rate capability of the MA-SCHC-20 electrode.

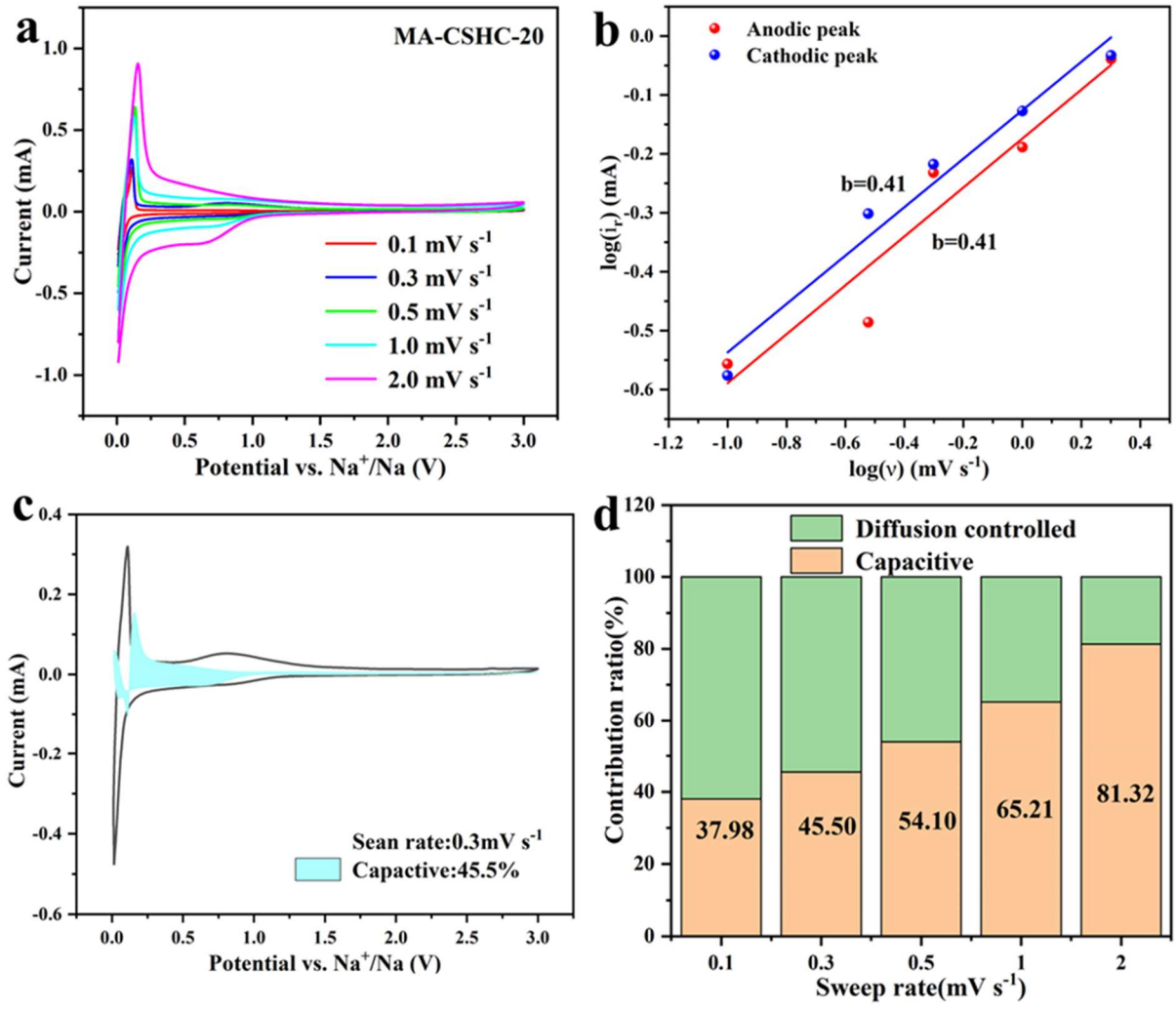

Figure 9. (a) CV curves of MA-SCHC-20 electrode at different scan rates, (b) b value calculated from the slope of log(scan rate) vs. log(peak current), (c) pseudocapacitive contribution percentage at a scan rate of 0.3 mV/s, (d) pseudocapacitive percentage at different scan rates

ISSN: 2414-1895 DOI: 10.6919/ICJE.202604_12(4).0054

4. Summary

In summary, this work presents a viable esterification-pyrolysis strategy for fabricating robust hard carbon anodes from tapioca starch. We established that incorporating maleic anhydride induces extensive cross-linking, which essentially increases the structural disorder and introduces oxygen-bearing groups to maximize Na^+ accommodation sites. Furthermore, tailoring the MA dosage to 20% successfully engineers a hierarchical porous morphology. This optimized framework is crucial for enhancing electrolyte saturation and expediting ion migration. Consequently, the resulting MA-SCHC-20 electrode exhibits outstanding long-term cyclability and a substantial reversible capacity of 350 mAh g^{-1}. Mechanistic analyses further indicate that the superior high-rate tolerance is predominantly driven by surface-induced pseudocapacitive adsorption, complemented by bulk diffusion intercalation. Broadly, this structural tailoring approach offers a compelling blueprint for converting economical biomass resources into advanced materials for commercial sodium-ion batteries.

Acknowledgments

Supported by the project of sci & tech of Zhongshan (2023A4011).

References

[1] Xie LJ, Tang C, Bi ZH, Song MX, Fan YF, Yan C, Li XM, Su FY, Zhang Q, Chen CM (2021) Hard carbon anodes for next generation Li-Ion batteries: review and perspective. Adv Energy Mater 11(38):2101650.

[2] Qin LN, Xu SD, Lu ZH, Wang L, Chen L, Zhang D, Tian J, Wei T, Chen JQ, Guo CL (2023) Cellulose as a novel precursor to construct high-performance hard carbon anode toward enhanced sodium-ion batteries. Diam Relat Mater 136:110065.

[3] Lu B, Zhang C, Deng DR, Weng JC, Song JX, Fan XH, Li GF, Li Y, Wu QH (2023) Synthesis of low-cost and high-performance dual-atom doped carbon-based materials with a simple green route as anodes for sodium-ion batteries. Molecules 28(21):7314.

[4] Morikawa Y, Nishimura S, Hashimoto R, Ohnuma M, Yamada A (2020) Mechanism of sodium storage in hard carbon: an X-ray scattering analysis. Adv Energy Mater 10(3):1903176

[5] Nobuhara K, Nakayama H, Nose M, Nakanishi S, Iba H (2013) First-principles study of alkali metal-graphite intercalation compounds. J Power Sources 243:585–587.

[6] Wang ZH, Selbach SM, Grande T (2014) Van der Waals density functional study of the energetics of alkali metal intercalation in graphite. Rsc Adv 4(8):4069–4079.

[7] Zhang LP, Wang W, Lu SF, Xiang Y (2021) Carbon anode materials: a detailed comparison between Na-ion and K-ion batteries. Adv Energy Mater 11(11):2003640.

[8] Irisarri E, Ponrouch A, Palacin MR (2015) Review-hard carbon negative electrode materials for sodium-ion batteries. J Electrochem Soc 162(14):A2476–A2482

[9] Komaba S, Murata W, Ishikawa T, Yabuuchi N, Ozeki T, Nakayama T, Ogata A, Gotoh K, Fujiwara K (2011) Electrochemical Na insertion and solid electrolyte interphase for hard-carbon electrodes and application to Na-ion batteries. Adv Funct Mater 21(20):3859–3867.

[10] Wu LM, Buchholz D, Vaalma C, Giffin GA, Passerini S (2016) Apple-biowaste-derived hard carbon as a powerful anode material for Na-ion batteries. ChemElectroChem 3(2):292–298

[11] Qiu S, Xiao LF, Sushko ML, Han KS, Shao YY, Yan MY, Liang XM, Mai LQ, Feng JW, Cao YL, Ai XP, Yang HX, Liu J (2017) Manipulating adsorption-insertion mechanisms in nanostructured carbon materials for high-efficiency sodium ion storage. Adv Energy Mater 7(17):1700403.

[12] Saavedra Rios C D M, Simone V, Simonin L, et al. Biochars from various biomass types as precursors for hard carbon anodes in sodium-ion batteries [J]. Biomass and Bioenergy, 2018, 117: 32-37.

[13] Yu P, Tang W, Wu F-F, et al. Recent progress in plant-derived hard carbon anode materials for sodium-ion batteries: a review [J]. Rare Metals, 2020, 39(9): 1019-1033.

ISSN: 2414-1895 DOI: 10.6919/ICJE.202604_12(4).0054

[14] Wang Q Q, Zhu X S, Liu Y H, et al. Rice husk-derived hard carbons as high-performance anode materials for sodium-ion batteries [J]. Carbon, 2018, 127:658-666.

[15] Qin L, Xu S, Lu Z, et al. Cellulose as a novel precursor to construct high-per form an ce hard carbon anode toward enhanced sodium-ion batteries [J]. Diamond and Related Materials, 2023, 136: 110065.

[16] Simone V, Boulineau A, De Geyer A, et al. Hard carbon derived from cell ulo seas anode for sodium ion batteries: Dependence of electrochemical properties on structure[J]. J Energy Chem, 2016, 25(5): 761-768.

[17] Chen Y, Li F, Guo ZY, Song ZQ, Lin YY, Lin W, Zheng LT, Huang ZG, Hong ZS, Titirici MM (2023) Sustainable and scalable fabrication of high-performance hard carbon anode for Na-ion battery. J Power Sources 557:232534.

[18] Buiel E, Dahn JR (1999) Li-insertion in hard carbon anode materials for Li-ion batteries. Electro chim Acta 45(1–2):121–130.

[19] Wang X, Huang LX, Zhang CH, Deng YJ, Xie PJ, Liu LJ, Cheng J (2020) Research advances in chemical modifications of starch for hydrophobicity and its applications: a review. Carbohyd Polym 240:116292

[20] Yan L, Wang J, Ren QJ, Fan LL, Liu BH, Zhang LJ, He L, Mei XX, Shi ZQ (2022) In-situ graphene-coated carbon microsphere as high initial coulombic efficiency anode for superior Na/K-ion full cell. Chem Eng J 432:133257.

[21] Song MX, Xie LJ, Cheng JY, Yi ZL, Song G, Jia XY, Chen JP, Guo QG, Chen CM (2022) Insights into the thermochemical evolution of maleic anhydride-initiated esterified starch to construct hard carbon microspheres for lithium-ion batteries. J Energy Chem 66:448–458.

[22] Song MX, Yi ZL, Xu R, Chen JP, Cheng JY, Wang ZF, Liu QL, Guo QG, Xie LJ, Chen CM (2022) Towards enhanced sodium storage of hard carbon anodes: regulating the oxygen content in precursor by low-temperature hydrogen reduction. Energy Storage Mater 51:620–629.

[23] Sun N, Guan ZRX, Liu YW, Cao YL, Zhu QZ, Liu H, Wang ZX, Zhang P, Xu B (2019) Extended "adsorption-insertion" model: a new insight into the sodium storage mechanism of hard carbons. Adv Energy Mater 9(32):1901351.

[24] Zhang SH, Sun N, Jiang MC, Soomro RA, Xu B (2023) Trash to treasure: sulfonation-assisted transformation of waste masks into high-performance carbon anode for sodium-ion batteries. Carbon 209:118034.

[25] Muruganantham R, Chiang YX, Liu WR (2022) Nitrogen-doped hard carbon derived from agro-food waste of mushroom bags biomass as an anode material for sodium-ion batteries. Mrs Energy Sustain 9(2):313–323.

[26] Sadezky A, Muckenhuber H, Grothe H, Niessner R, Pöschl U (2005) Raman micro spectroscopy of soot and related carbonaceous materials: spectral analysis and structural information. Carbon 43(8):1731–1742.

[27] Jeon JW, Sharma R, Meduri P, Arey BW, Schaef HT, Lutkenhaus JL, Lemmon JP, Thallapally PK, Nandasiri MI, McGrail BP, Nune SK (2014) In situ one-step synthesis of hierarchical nitrogen-doped porous carbon for high-performance supercapacitors. Acs Appl Mater Inter 6(10):7214–7222.

[28] Jeon JW, Zhang LB, Lutkenhaus JL, Laskar DD, Lemmon JP, Choi D, Nandasiri MI, Hashmi A, Xu J, Motkuri RK, Fernandez CA, Liu J, Tucker MP, McGrail PB, Yang B, Nune SK (2015) Controlling porosity in lignin-derived nanoporous carbon for supercapacitor applications. Chemsuschem 8(3):428–432.